SPE-205142-MS

Development of Time Lapse VSP Integration Workflow: A Case Study at Farnsworth CO_2-EOR Project

Marcia McMillan, New Mexico Institute of Mining and Technology; Robert Will, Petroleum Recovery Research Center; Tom Bratton, Tom Bratton LLC; William Ampomah and Hassan Khaniani, Petroleum Recovery Research Center

This paper was prepared for presentation at the SPE Europec featured at 82nd EAGE Conference and Exhibition held in Amsterdam, The Netherlands, 18 - 21 October 2021.

Abstract

This study aims to develop a 4D Vertical Seismic Profile (VSP) integration workflow to improve the prediction of subsurface stress changes. The selected study site is a 5-spot pattern within the ongoing CO_2-EOR operations at the Farnsworth Field Unit FWU in Ochiltree County, Texas. The specific pattern has undergone extensive geological and geomechanical characterization through the acquisition of 3D seismic data, geophysical well logs, and core.

This workflow constrains a numerical hydromechanical model by applying a penalty function formed between "modeled" versus "observed" time-lapse compressional and shear seismic velocity changes. Analyses of geophysical logs and ultra-sonic measurements on core exhibit measurable sensitivities to changes in both fluid saturation and mean effective stress. These data are used to develop a site-specific rock physics model and stress-velocity relationship, which inform the numerical models used to generate the "modeled" portion of the penalty function. The "observed" portion of the penalty function is provided by a novel elastic full-waveform inversion of the available 3D baseline and three monitor surveys to produce high-quality estimates of time-lapse compressional and shear seismic velocity changes.

The modeling workflow accounts sequentially for fluid substitution and stress impacts. Hydrodynamic and geomechanical properties of the 3D coupled numerical model are estimated through geostatistical integration of well log and core data with 3D seismic inversion products. Changes in seismic velocities due to fluid substitution are computed using the Biot-Gassmann workflow and site-specific rock physics. Stress impacts on time-lapse seismic velocity changes are modeled from the effective stress output of the hydromechanical model and are initially based on the velocity versus effective stress relationship extracted from core mechanical testing.

Based on the principle of superposition of seismic wavefields, seismic velocity changes attributed to fluid substitution and that due to changes in mean effective stress are treated as linearly additive. The modeled results are upscaled using Backus averaging to reconcile scale discrepancies between the modeled and measured datasets to formulate the penalty function.

This manuscript presents the forward modeling process and concludes that for the base case, the seismic velocity changes due to mean effective stress dominates over the seismic velocity changes attributed to fluid substitution because of the extensive range of the pressure perturbations. Successful minimization of this penalty function calibrates the coupled hydrodynamic geomechanical numerical model and affirms the suitability of acoustic time-lapse measurements such as 4D-VSP for geomechanical calibration.

Introduction

Technological advancement in Carbon Capture and Storage (CCS) and Carbon Capture Utilization and Storage (CCUS) are of the utmost importance, as minimizing atmospheric concentrations of CO_2 is essential for mitigating against global temperature rise (Boot-Handford et al., 2014; Kheshgi, de Coninck, & Kessels, 2012; Rubin & De Coninck, 2005).

CCS typically involves the injection of captured CO_2 in deep saline reservoirs (Bachu, 2008), but CCS project implementation requires significant capital investments (Heddle, Herzog, & Klett, 2003; Mechleri, Brown, Fennell, & Mac Dowell, 2017) as well as public buy-in (De Coninck, Stephens, & Metz, 2009). In contrast, CO_2-EOR as CCUS provides the advantages of existing infrastructure and expertise (Jacobs, 2020; Núñez-López & Moskal, 2019) and is inherently more profitable as CO_2-EOR operations lead to increased oil production (Verma 2015). Many oil and gas companies have formulated plans to move their operations towards NET Zero Carbon emissions (Ben van Beurden, 2020; Josu Jon Imaz, 2019; Patrick Pouyanné, 2020); governmental agencies, recognizing the need to quell global warming, incentivize permanent CO_2 storage with tax credits (Grant 2019). Several nations are actively investigating CCUS implementation, in part, to curb their total greenhouse gas emissions by 2050 (Hares, 2020; Kokal, Sanni, & Alhashboul, 2016; Suicmez, 2019).

Several authors (Hawkes, McLellan, & Bachu, 2005; Hillis, 2001; Streit & Hillis, 2004) have documented the increased geomechanical risks associated with CCUS due to the repressurization of partially depleted zones, and the need for stringent monitoring of CO_2-EOR processes have been well established (Hovorka et al., 2018). Monitoring techniques for several ongoing CO_2-EOR include InSAR evaluations (Morris, Hao, Foxall, & McNab, 2011; Ringrose et al., 2013; Rutqvist, Vasco, & Myer, 2010), microseismic monitoring (Wilson et al., 2004), time-lapse 3D seismic and time-lapse VSP measurements (Huang, Juhlin, Kempka, Norden, & Zhang, 2015).

The work of Olden (2001), Herwanger (2005), and Vidal (2002) have long established that measured time-lapse seismic measurements carry the combined effects of both fluid saturation changes and subsurface stress state changes. Time-lapse seismic measurements provide tremendous benefits, as each measurement represents a snapshot of the reservoir saturation and stress state and can be used for ground-truthing.

Assessing stress state evolution is of extreme importance in assuring CO_2 containment for CCUS projects. This theory forms the basis for this current work as the ultimate goal is to improve the stress calibration within the interwell space by using a time-lapse VSP measurements.

The study is performed within a 5-spot pattern of the ongoing CO_2-WAG operations within the Farnsworth Field Unit (FWU). Southwest Regional Partnership for Carbon Sequestration (SWP) studies the geologic (Gallagher, 2014; Rose-Coss, 2017), hydrodynamic (Ampomah et al., 2016), geomechanical (Trujillo, 2018), and chemomechanical impacts (Wu et al., 2018) of CO_2 injection and storage at FWU. As of August 2020, the FWU has permanently stored 1.38×10^6 Mt. The FWU must permanently sequester these large volumes of CO_2. Additionally, the current average reservoir pressure is estimated at greater than twice the reservoir pore pressure at discovery even though initially underpressured, introducing significant concerns over the storage containment integrity.

The current geomechanical study at FWU seeks to develop a time-lapse VSP integration workflow aimed at subsurface stress calibration. The forward modeling procedure requires calibrated reservoir simulation and coupled geomechanical simulation model results. Seismic velocity attributed to fluid substitution and

that due to stress changes is computed and summed to form the modeled portion of the penalty function. The observed part of the penalty function is provided by the novel waveform inversion performed by Los Alamos National Labs (LANL). The mismatch is determined by differencing the observed seismic velocities from the modeled seismic velocity.

Minimizing this mismatch is the key to successful stress calibration and provides answers regarding the relative contributions to seismic velocity changes for fluid substitution and subsurface stress state at each monitor time-lapse period of this particular study? Ultimately, the question this work addresses is: Are repeat acoustic measurements such as VSP appropriate for the predictions of stress changes, and if so, under which circumstances?

Statement of Theory and Definitions.

The current geomechanical study seeks to calibrate a coupled hydrodynamic-geomechanical simulation model for observed time-lapse VSP measurements. The time-lapse VSP records the combined effects of fluid substitution and subsurface pore pressure changes. This section covers the relevant theoretical background of the seismic wave equation and derives the relationships for shear and compressional seismic velocities. Background knowledge on seismic velocity changes attributed to fluid substitution and due to pore pressure changes is also presented.

Stress, Strain, and Seismic Wave Velocity

Seismic waves can be thought of as the propagation of energy through an elastic medium as it travels from its source. The seismic wave equation is the result of coupling of Newton's second law and stress-strain relationships given by,

$$\sigma_{ij,j}(x,t) = \rho \frac{\partial^2 u_i(x,t)}{\partial t^2} \quad \text{eq. 1}$$

Where σ is the stress, i, j =1, 2, 3 with the Einstein summation convention, ρ is density, t is time, u is displacement. In an elastic medium, Hooke's Law is defined by,

$$\sigma_{ij} = c_{ijkl}\varepsilon_{kl} \quad \text{eq. 2}$$

where ε_{kl} is defined as,

$$\varepsilon_{kl} = \frac{1}{2}\left(u_{k,1} + u_{1,k}\right). \quad \text{eq. 3}$$

Particle displacements for compressional seismic wave are parallel to propagation direction, while for shear seismic waves, particle displacements are perpendicular to the direction of propagation. The relationship for compressional P-wave seismic velocity (V_p) is shown in equation 4, and equation 5 is the expression for shear seismic velocity,

$$V_P = \sqrt{\frac{K + 4\mu/3}{\rho}} \quad \text{eq. 4}$$

$$V_S = \sqrt{\frac{\mu}{\rho}} \quad \text{eq. 5}$$

Shear and compressional seismic velocities are explicit functions of elastic moduli (saturated Bulk Modulus and Shear Modulus) and formation density, both factors that are altered during the CO_2-WAG operations and which ought to impact measured observed seismic velocities.

Seismic Velocity: Impacts of Fluid Substitution

The Biot Gassman workflow (Biot, 1956; Gassmann, 1951) models fluid effects on seismic velocities by computing the saturated elastic moduli and bulk formation density. Fundamental assumptions of the

Biot Gassmann workflow includes homogeneous, isotropic, and connected porous media. An additional assumption is that the acoustic waves propagate through the formation at low frequencies such that the seismic waves do not trigger pressure disequilibration within the pore spaces, at scales much smaller than the wavelength.

Equations 6, 7, 8, and 9 calculate the constituent elastic moduli and Bulk density for shear and compressional seismic velocity. The formation bulk density is the volume-weighted average of the rock matrix and fluid densities expressed in equation 6 (Batzle & Wang, 1992). Fluid density and saturation are extracted from the dynamic reservoir simulation model for each time-lapse time step. Equation 7 infers that the impact of changing pore fluids on the shear modulus is minuscule, and the saturated shear modulus to be set equal to the dry shear modulus.

We used the following equations 8 and 9 to determine the change in Bulk Modulus due to changes in fluid contents:

$$\rho_{Bulk} = \rho_{matrix}\ (1-\phi) + \phi\left(\rho_o S_o + \rho_g S_g + \rho_w S_w\right), \quad \text{eq. 6}$$

$$\mu_{sat} = \mu_{dry}\,, \quad \text{eq. 7}$$

$$K_f = \frac{1}{c_f} \quad \text{eq. 8}$$

$$K_{sat} = K_{fr} + \frac{\left[1 - \frac{K_{fr}}{K_s}\right]^2}{\frac{\phi}{K_f} + \frac{(1-\phi)}{K_s} - \frac{K_{fr}}{K_s^2}}, \quad \text{eq. 9}$$

where: φ is the matrix porosity, and S represents fluid saturation. The subscripts w, o, g represent water, oil, gas, respectively. K represents the bulk modulus with subscripts sat, fr, s, and f representing the saturated porous medium, the dry rock frame, the constituent solid grains, and the pore-filling fluid. c_f is the total fluid compressibility.

The porosity, the solid constituent grain, dry rock frame, and the pore-filling Bulk Modulus all affect the saturated Bulk Modulus. Equation 8 shows that the fluid bulk modulus computed at every time-lapse time-step from the total fluid compressibility extracted from the dynamic reservoir simulation model. Equation 9 is the final expression for the saturated Bulk Modulus of the porous medium.

Krief model Rockframe Elastic Moduli. Our target formation, Morrow B is highly heterogenous due in part to dispersed clay deposited during its diagenetic evolution (Rose-Coss, 2017; Rose-Coss et al., 2015). Several studies have shown the unpredictable impacts of clay content on the Biot-Gassmann workflow results (Han, Nur, & Morgan, 1986; Tosaya, 1983; Vanorio, Prasad, & Nur, 2003). Consequently, the appropriate implementation of Biot Gassmann requires the development of a relationship between the properties of the rocks' composite grains and the rock frame, aptly expressed through the Biot poroelastic coefficient (eq. 10) Geertsma (1957) and Skempton (1961),

$$K_{fr} = (1-\alpha)K_s. \quad \text{eq. 10}$$

This study benefits from a site-specific Krief rock physics model. Krief (1990) studied the relationships between elastic (Bulk Modulus and Shear Modulus) moduli and porosity for water-saturated sandstones (eq. 11), developing the following empirical equation. The coefficient n is the linear tangent slope on the elastic moduli versus porosity plot, for Krief's study n =3,

$$\alpha = 1 - [1-\phi]^{\left(\frac{n}{1-\phi}\right)}. \quad \text{eq. 11}$$

Substitution of the Biot poroelastic coefficient into eq. 9 yields an equivalent expression for saturated bulk modulus given by

$$K_{sat} = K_{fr} + \frac{\alpha^2}{\frac{\phi}{K_f} - \frac{(\alpha-\phi)}{K_s}} \quad \text{eq. 12}$$

Seismic Velocity: Impacts of Pore Pressure Change

Shear and compressional seismic velocities are affected by changes in subsurface pore pressure. The reservoir is a poroelastic medium on which imposed loads can deform the connected pore spaces, the rock matrix's fabric, or both. The reservoirs' rock matrix is restricted from volume deformation by the surrounding tectonic forces. Consequently, modifications to the pore pressure affect the normal-stresses applied to the inside of the pore surfaces: dilation for pore pressure increase and contraction for pore pressure decrease. Essentially, the pore pressure bears a portion of any imposed load (Biot, 1955),

$$\sigma'_{ij} = \sigma_{ij} - \alpha\delta_{ij}P, \quad \text{eq. 13}$$

$\sigma ij'$ is the effective stress, α is the poroelastic Biot coefficient, which scales the impact of the pressure pore (P) change. Expanded or contracted pore space ultimately impacts the bulk density and the Bulk Modulus of the formation through which the seismic waves travel. These property modifications inherently cause changes to the shear and compressional seismic velocities. This link between pore pressure changes, stress changes, and seismic velocity changes is well known (Birch 1961, Nur and Simmons 1969) and has been thoroughly explored by laboratory studies (Eberhart-Phillips, Han, et al. 1989, Mese 2005). The laboratory studies utilize a confining pressure akin to the overburden pressure. The opposing effects of confining pressure and pore pressure align with Equation 13. Empirical relationships between seismic velocity and stress have been devised (Dobróka and Molnár 2012). This study of the ongoing CO_2-WAG operations within the Morrow B benefit from similar ultrasonic measurements, thereby relating changes in effective pressure to shear and compressional seismic velocity.

Field Description and Production History

The study area for this time-lapse Vertical Seismic Profile (VSP) study is a 5-spot pattern within the Western FWU's ongoing CO_2-EOR operations. The selected injection pattern is centered on the characterization well, which has undergone extensive geological and geomechanical characterization through geophysical well logs and core. In combination with existing 3D surface seismic data, the property population for critical geomechanical parameters has been devised (McMillan, Will, Ampomah, Balch, & Czoski, 2019). Figure 1 shows the Western FWU with overlays of the sector region covering the 5-spot pattern, the outline of the acquired time-lapse VSP datasets, and the 1000 ft radius around the 13-10 A where the penalty function is computed.

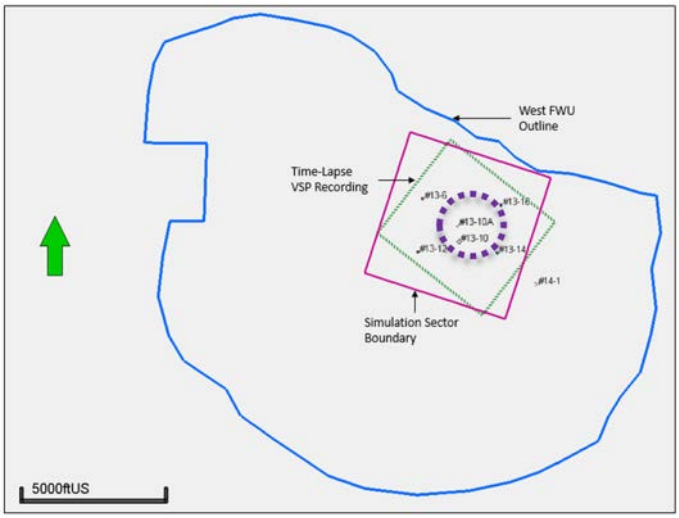

Figure 1—Relative Location of Simulation Sector Model and Acquired Time-Lapse VSP Datasets.

Figure 2 shows the stratigraphic column over the storage complex. These formations are Pennsylvanian in age and include the Atokan Thirteenfinger Limestone and Morrowan Morrow Shale seals, which overlay the Morrow-B formation. The Morrow-B serves dually as the production and storage zone and ranges in thickness between 0 and 54 feet with an average thickness of 29 feet (Munson, 1988). The underlying formations are interchanging Morrowan sandstone and shale.

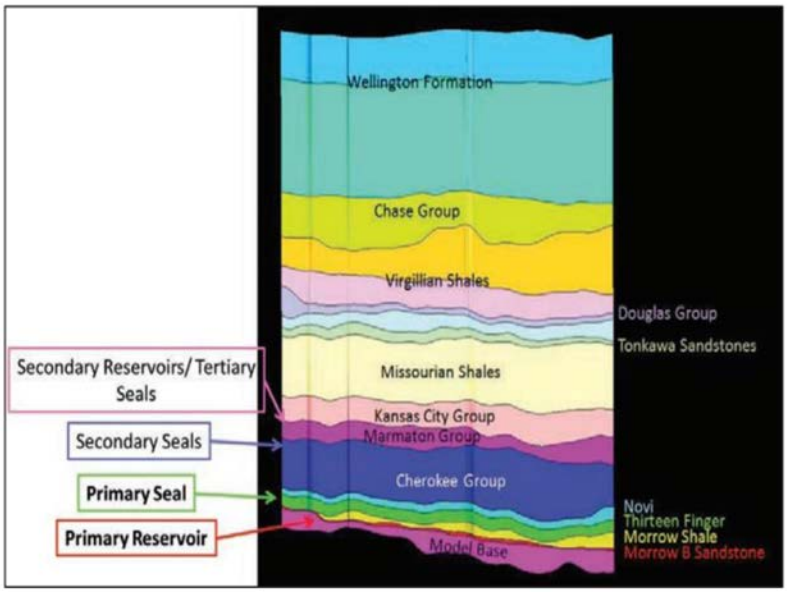

Figure 2—Stratigraphy of Morrow-B Storage Complex

The Morrow-B formation has been subjected to three different production methodologies. Primary depletion began in 1955 and continued until the gradual west to east implementation of the waterflood starting in 1964. The waterflood period was extensive, continuing until December 2010 with the phased implementation of the current CO_2-WAG EOR. The pressure maintenance schemes have been set up as 5-spot patterns. This complicated production history has resulted in large increases in average reservoir pressure, as shown in Figure 3 below. The Morrow-B was under pressured at 2217 psia at discovery and naturally saw declining pressures during depletion production. The simulation model over the waterflood period showed significant increases in pore pressure, to over 4950 psia, while the CO_2-WAG shows shallow

pressure perturbations. Recent BHP measurements indicate that the BHP of the fields injector wells are not restricted to a maximum BHP of 5000 psi as reflected in prior modeling work (similar to Figure 3) but may, in some cases, exceed 6000 psi. Inherently, every pressure modification triggers a change in the subsurface stress state. These high injection pressures and the large volumes of CO_2 injected advocate for a comprehensive geomechanical study.

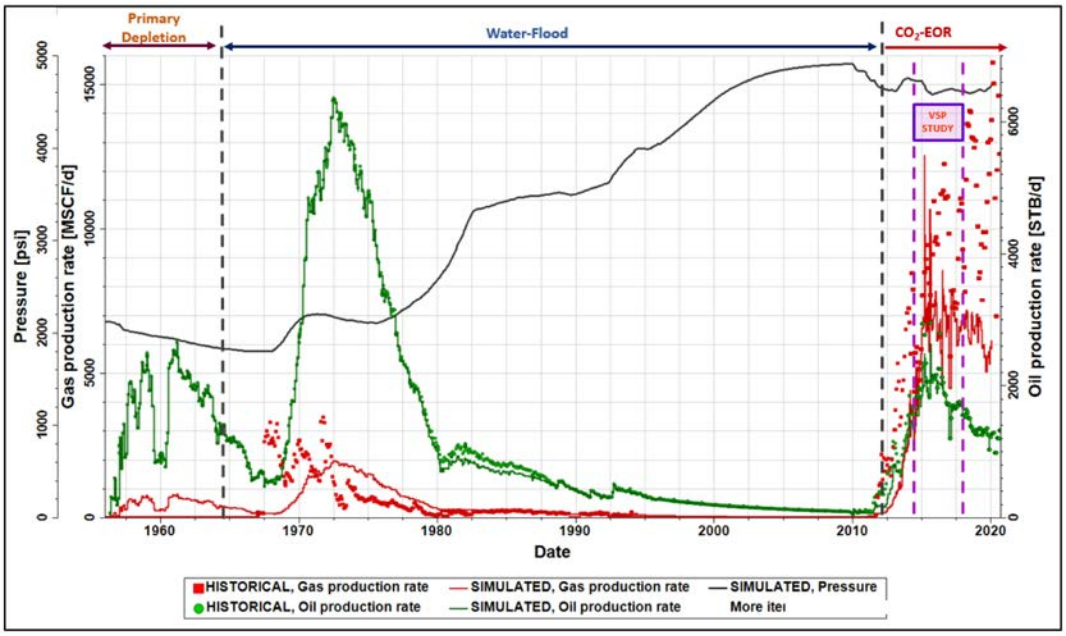

Figure 3—Morrow B Production History with Period of Time-Lapse Study Highlighted

Available Datasets

Time-Lapse VSP Acquisition

The physical state of a porous material: temperature, pressure, the potential presence of cracks, and the pore fulfilling fluids impact the propagation of seismic waves through that medium. Repeated seismic measurements covering the same region over elapsed time-periods can indicate changes in the subsurface conditions. This project utilizes these principles to assess the time-lapse VSP study over the ongoing CO_2-WAG operation at FWU.

Surface activities within the FWU preclude access to specified ground locations (Figure 4b), and seismic simulation aids in developing the effective 3D VSP acquisition design. Figure 4a shows the modeling software utilized and highlights the angle of incidence at which the elastic waves intersect the mapped Morrow B identifies the 1000-ft radius around the 13-10A used as observed data for the penalty function.

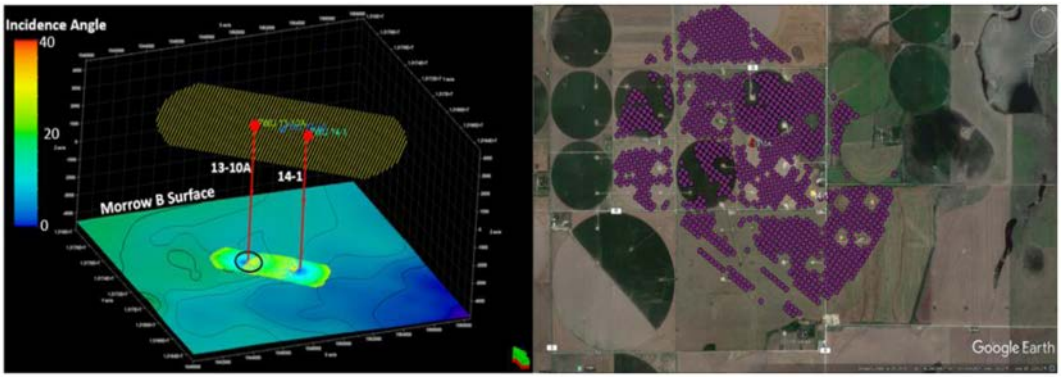

Figure 4—a) Seismic imaging illumination map for 3D VSP acquisition b) Source Locations Impounded by the Vibroseis Truck

VSP was acquired using a vibroseis truck, and Figure 4b illustrates the locations where the ground surface is impounded to generate seismic waves. Forty-level, 3 component geophones with 50-foot interval spacing were present in both the 13-10A and 14-1 wells. FWU VSP baseline survey acquisition occurs in February 2014, followed by three subsequent surveys:

Monitor 1 in January 2015,

Monitor 2 in November 2016,

Monitor 3 in December 2017.

These effective 3D seismic measurements were inverted for shear and compressional seismic velocities by LANL using a novel waveform inversion. Subsequent computation of each of the three time-lapse seismic velocity volumes is relative to the VSP baseline survey. Figure 5 shows the resulting shear and compressional seismic velocities at the Morrow-B surface (-4650 SSTVD, 7800 TVD ft; 1417.3 mSSTVD, 2377.3 TVD m).

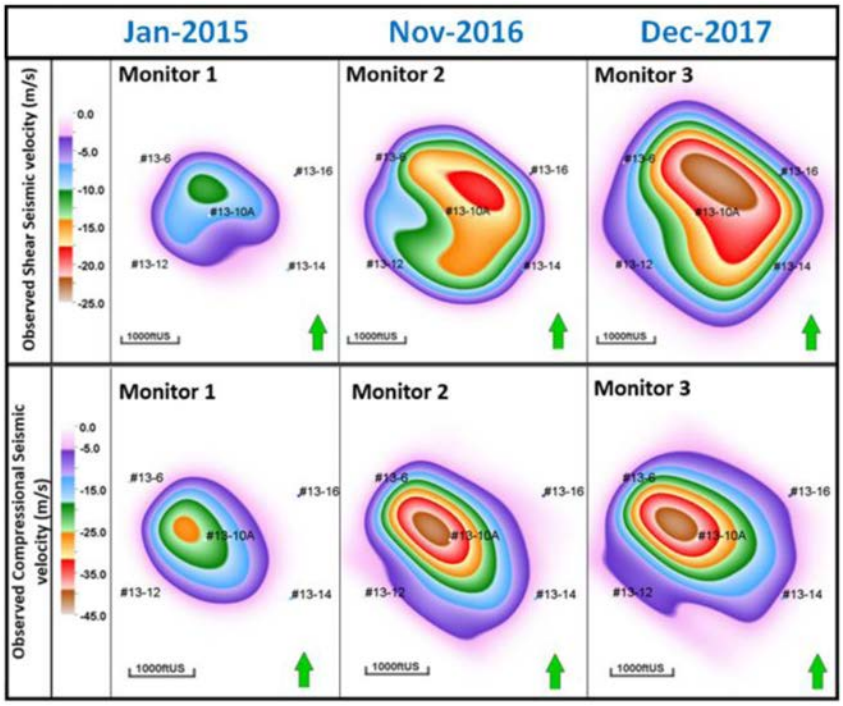

Figure 5—Time slice of inverted shear and compressional seismic velocity on the Morrow B Formation surface.

Later, after detecting the stress rotation in the shallow borehole through geophysical log analysis, an anisotropic elastic waveform inversion algorithm was applied utilizing 1D models of Thomsen parameters

Epsilon and Delta extracted from the wellbore geophysical logs. This inversion is consistent with both the stress rotation and constitutive relations. As anticipated, the results show the temporal-spatial evolution of shear and compressional velocities with an increased injection of CO_2.

Site-Specific Rock Physics Relationship

The site-specific rock physics relationship is based on the Krief model discussed in section 2.2.2 and is the essential link allowing for the implementation of the Biot-Gassmann workflow. The Krief site-specific rock physics is developed by investigating the relationships between Shear Modulus and Bulk Modulus, derived from geophysical logs, and the formation porosity. Figure 6a shows the Shear modulus plot versus formation porosity, with the red line defining an average fit. The y-axis intercept of the red line corresponds with μ_{smean}, the shear modulus for zero porosity (μ_s) given by equation 14a. Similarly, an empirical relationship for the dry rock frame shear modulus as a function of porosity is provided by Equation 14.b. Utilizing the formation porosity, the distribution for the dry rock frame's shear modulus is determined as a function of porosity,

$$\mu_s = 1.455370\phi + \mu_{s_{mean}}, \quad \text{eq. 14a}$$

$$\mu_{fr} = 5.276995\phi + \mu_s. \quad \text{eq. 14b}$$

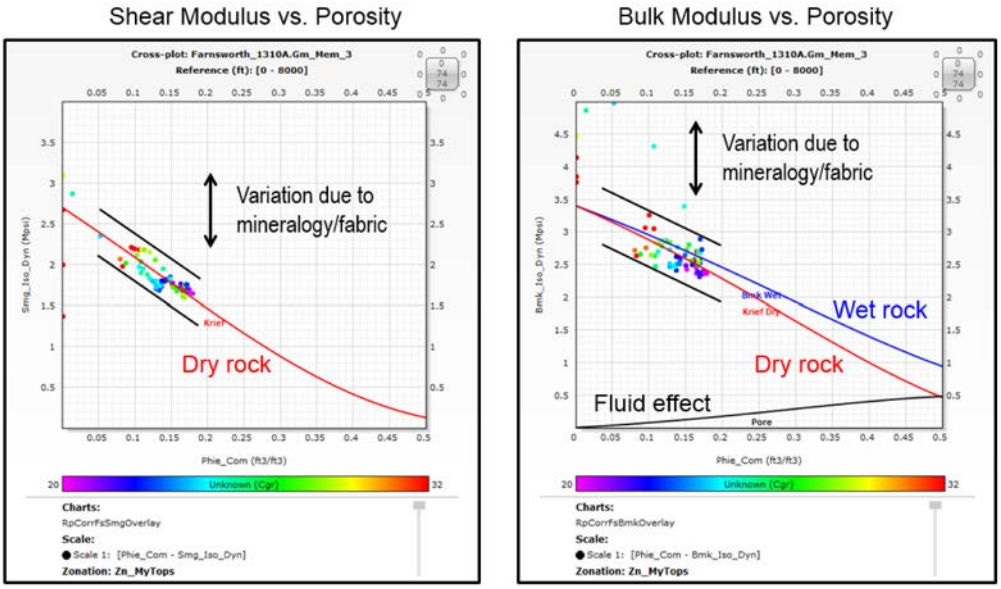

Figure 6—Development of Krief Rock Physics Relationship for Morrow-B formation. Figure 6a shows the Shear Modulus versus porosity, while figure 6b shows the bulk Modulus

Similar relationships are developed from Figure 6b for the bulk moduli relationships as a function of porosity and are shown as equations 15a and 15b. The bulk modulus relationship for the dry rock frame (K_{fr}) and the mineral grains (K_s) are used to define the Biot poroelastic coefficient based on equation 10. The Biot poroelastic coefficient ultimately impacts the seismic velocity due to fluid substitution as well as the seismic velocity due to mean effective stress change,

$$K_s = 1.520044\phi + K_{s_{mean}}, \quad \text{eq. 15a}$$

$$K_{fr} = 5.801835\phi + K_s. \quad \text{eq. 15b}$$

The solid black lines in Figure 6a and 6b constrain the potential variations due to the rock matrix mineralogical and fabric variations, and their extrapolated intersections with the y-axis serve as the minimum and maximum values for μ_{smean} and K_{smean}.

Effective Stress to Seismic Velocity Response

Figure 7 shows the results of the ultrasonic velocity testing on the retrieved Morrow B core. Figure 7a shows the relationship between compressional seismic velocity and mean effective stress, while 7b addresses the shear seismic velocity relationship with mean effective stress. Both graphs illustrate that for mean effective states of 1750 psi and 2750 psi, a linear correlation exists between the mean effective stress and the shear and compressional seismic velocity. The mean effective stress to seismic velocity correlation is the vehicle by which the results from the coupled hydrodynamic geomechanical simulation model are converted to seismic velocities.

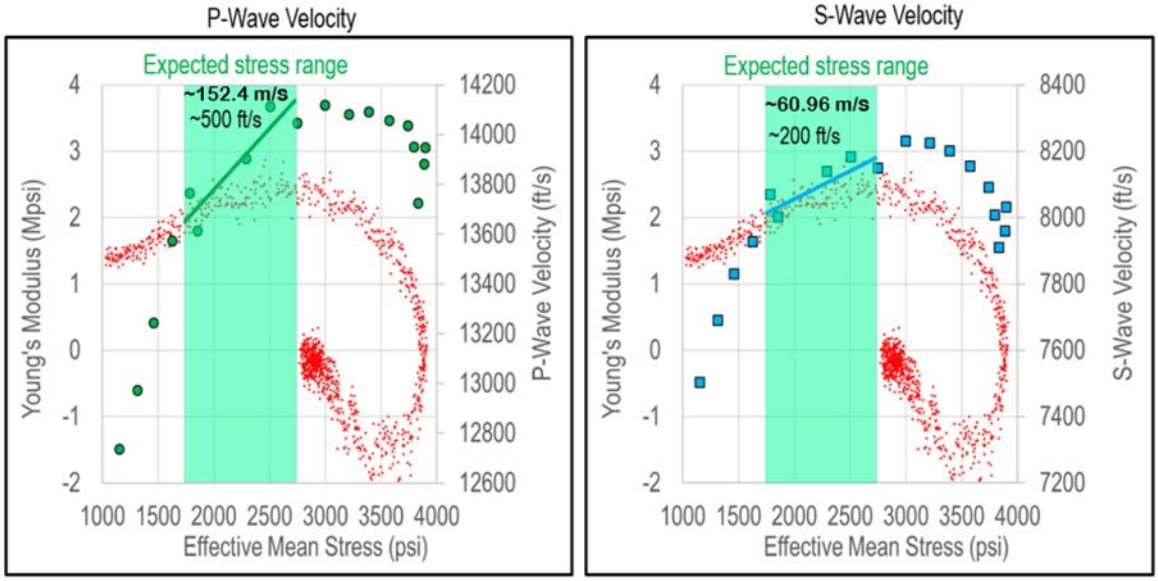

Figure 7—Ultrasonic seismic response of core gives a direct correlation between mean effective stress changes and changes in shear and compressional seismic velocity.

The dynamic coupled hydrodynamic-geomechanical simulation model uses the influx induced pressure distributions extracted from the compositional reservoir simulation model to compute stress changes. Equation 16 shows the relationship for mean effective stress based on the effective stresses in the x, y, and z cartesian directions extracted from the geomechanical simulation model. Equations 17 and 18 compute the changes in shear and compressional seismic velocity due to subsurface stress changes,

$$\sigma'_{mean} = \left(\sigma'_{11} + \sigma'_{22} + \sigma'_{33}\right)/3, \quad \text{eq. 16}$$

$$dV_P, \quad m/s = \frac{500}{3.28}\left(\frac{\Delta\sigma' mean}{1000}\right), \quad \text{eq. 17}$$

$$dV_S, \quad m/s = \frac{200}{3.28}\left(\frac{\Delta\sigma' mean}{1000}\right), \quad \text{eq. 18}$$

where σ' is the effective stress, and the subscripts mean refers to the mean effective stress, dV_p represents the change in compressional seismic velocity, and dV_s is shear seismic velocity. The inclusion of Youngs' Modulus in Figure 7 is a further indication of the non-linear relationships existing outside of the previously described narrow linear range.

Methods

The study seeks to improve the prediction of subsurface stresses in the inter-well spaces by minimizing the mismatch between the "observed" and "modeled" shear and compressional seismic velocities. The novel full-wave inversion (Gao & Huang, 2019) of the acquired time-lapse VSP measurements performed by

Los Alamos National Labs serves as the observed dataset. The forward modeling workflow outlined in Figure 8 provides the "modeled" portion of the penalty function. In brief, the linear summation of seismic velocity change attributed to fluid substitution and that due to subsurface stress changes form the "modeled" portion of the penalty function. Seismic velocity due to stress is derived from the coupled hydrodynamic-geomechanical simulation model. At the same time, that fluid substitution comes from the compositional reservoir simulation model.

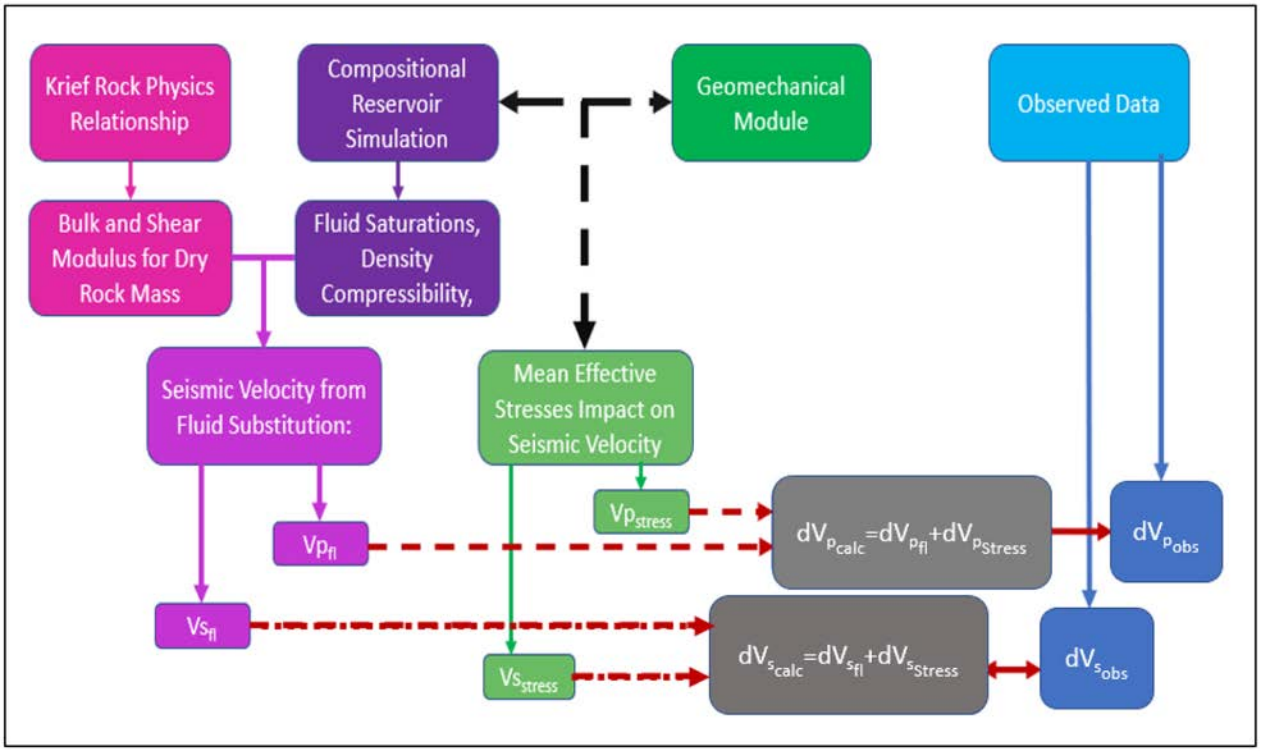

Figure 8—Integrated workflow used for prediction of subsurface stresses using mismatch between the "observed" and "modeled" seismic velocities.

Compositional Reservoir Simulation Model

An overview of the Morrow B production history has been covered in section 3. The portion of the compositional reservoir simulation pertinent to the time-lapse VSP under consideration spans from January 2014, the time of the drilling of the 13-10A well up to January 2018 after acquiring the monitor 3 VSP. The compositional reservoir simulation of the CO_2-WAG utilized distinct relative permeability relationships (Rasmussen, Fan, et al. 2019) for the individual HFU discretization initially described by Ross-Coss (2015).

The area of interest is only one selected 5-spot pattern (Figure1). Sector modeling is implemented to reduce the computation load. Fluid saturation, density, and total fluid compressibility at the baseline and monitor times are extracted from the calibrated simulation model for implementation in the Biot-Gassmann workflow.

Seismic Velocity Attributed to Fluid Substitution

Computations of shear and compressional seismic velocity use the Biot-Gassmann workflow reviewed in section 2.2. Fluid saturations and fluid densities are extracted at the baseline VSP, and every monitor time-step and used to compute the formation bulk densities (eq.6). The dry rock frame elastic moduli are calculated using the site-specific Krief rock physics relationships (section 4.2). Equations 14 a, b compute the shear modulus, while equation 15 a, b compute the dry frame Bulk modulus.

Equation 7 indicates that the saturated shear modulus is equal to the dry shear modulus. The computation of the saturated Bulk Modulus (eq. 12) requires the fluid Bulk Modulus (K_f), which is computed by inverting the total fluid compressibility (eq.8). The Biot poroelastic coefficient is calculated from the bulk modulus ratio of the constituent minerals' rock frame and bulk modulus (eq.10). These preceding equations compute all the required inputs for the final computation of the shear (eq. 5) and compressional seismic velocity (eq. 4) attributed to fluid substitution.

Geomechanical Simulation Model Linear Elastic Assumption

The static MEM model extends from the surface to 17,000 ft TVD at the bottom of the under-burden. The geomechanical model dimensions are 204 by 194 by 87 cells. The mechanical property population is generated through the geostatistical integration of well-log and core data with 3D seismic inversion products.

Similar to the compositional reservoir simulation, the geomechanical simulation is performed only within the simulation sector boundary (Figure 1). For computational efficiency, sector boundary conditions are defined relative to the full field geomechanical simulation model. The geomechanical sector simulation also implements the simplifying assumption of linear elasticity. The tenets of linear elasticity mean the geomechanical model properties have only two degrees of freedom. Consequently, the previously determined distributions for the saturated bulk modulus and saturated Shear modulus, computed within the producing Morrow B interval, inherently define the corresponding elastic moduli. Poisson ratio and Young's moduli are determined from the saturated bulk Modulus and Shear modulus using equations 19 and 20.

For consistency, the same Biot coefficient applied for the computation of seismic velocity attributed to fluid saturation is imposed. The final geomechanical grid merges property distributions determined through the geostatistical integration with the property population within the simulation sector boundary where the linear elastic assumption is applied.

$$E = \frac{9K_{sat}\mu_{sat}}{3K_{sat} + \mu_{sat}} \quad \text{eq. 19}$$

$$v = \frac{3K_{sat} - 2\mu_{sat}}{2\left(3K_{sat} + \mu_{sat}\right)} \quad \text{eq. 20}$$

E is the Youngs modulus, ν is the Poisson ratio, and the subscript *sat* refers to the saturated elastic modulus.

The geomechanical simulation's remaining input parameters are the pressure distribution grids derived from the calibrated reservoir simulation (hydrodynamic) model. The hydrodynamics are coupled one-way with the 3D MEM to create the dynamic geomechanical model. Although we recognize the non-uniqueness of calibrated reservoir simulation, we utilize only one hydrodynamic solution. Pressure distributions from the calibrated reservoir simulation model at the simulation start time (1-Jan-2014), the baseline, and three monitors are extracted and fed to the geomechanical model. The geomechanical simulation is a function of pressure, sector model boundary conditions, and the geomechanical property population: elastic moduli and Biot poroelastic coefficient.

Effective Stress and Seismic Velocity

The geomechanical sector utilizes the pressure grids from the calibrated simulation model to performs a one-way coupling, which updates the subsurface stress states. The normal stresses in the cartesian directions (x,y,z) at the baseline and monitor measurements are extracted to compute the effective stress state within the reservoir interval (eq.16). Changes in effective stress state are calculated relative to the baseline for every monitor measurement. Figure 7 illustrates direct correlations between effective stress change and shear (equation 18) and compressional (equation 17) seismic velocity changes.

Linear Summation

Based on the principle of superposition of seismic wavefields, the changes in shear and compressional time-lapse seismic velocities attributed to fluid substitution and the changes due to subsurface stress changes are linearly additive. Their sum (eq. 21) represents the modeled portion of the penalty function,

$$dV^{monitor}{}_{modeled} = dV^{monitor}{}_{fluid} + dV^{monitor}{}_{stress}, \quad \text{eq. 21}$$

where dV refers to dVs and dVp. the superscript monitor refers to the three monitor VSP surveys acquired in this study.

Formulation of Penalty Function

After scaling the modeled input, the penalty function is represented by equations 22.

$$f = \left(d^{cal} - d^{obs}\right). \quad \text{eq. 22}$$

The penalty function in Equation 21 measures the mismatch (f) between the modeled and observed seismic velocity. The observed portion of the penalty function is provided by the novel full-waveform inversion performed by LANL (Kai and Lianjie, 2019). The wavelength of the "observed" time-lapse VSP velocities are on the order of 200 ft-300 ft (60.96 m - 91.44m), leading to resolutions that range from 50 ft to 75 ft (15.24 m – 22.86m). The producing Morrow B interval is subdivided into four layers and ranges in thickness from 0 to 59 ft with a mean 29 ft. Backus average of the modeled portion of the penalty function is applied to reconcile the differences in scale.

Results and Discussion

The current study seeks to develop a time-lapse VSP integration workflow aimed at subsurface stress calibration. We seek to formulate the modeled equivalent by extracting and utilizing fluid properties and mean effective stress for the forward modeling of shear and compressional seismic velocities attributed to fluid substitution changes as well as due to changes in mean effective stress.

Compositional Reservoir Simulation

The forward modeling workflow begins with the compositional reservoir simulation. The time-lapse VSP study spans January 2014 to January 2018, the segment of the production history match captured in Figure 9. The production methodology implemented during this period is the CO_2-WAG process, which seeks to enhance oil recovery by swelling the in-situ oil and mobilizing production while simultaneously storing injected CO_2. Alternating water and CO_2 injection at predetermined intervals provide pressure maintenance. These production and injection patterns cause the mixing of pore fluids, changing saturation conditions with time, and inherently impact the measured time-lapse shear and compressional seismic velocities.

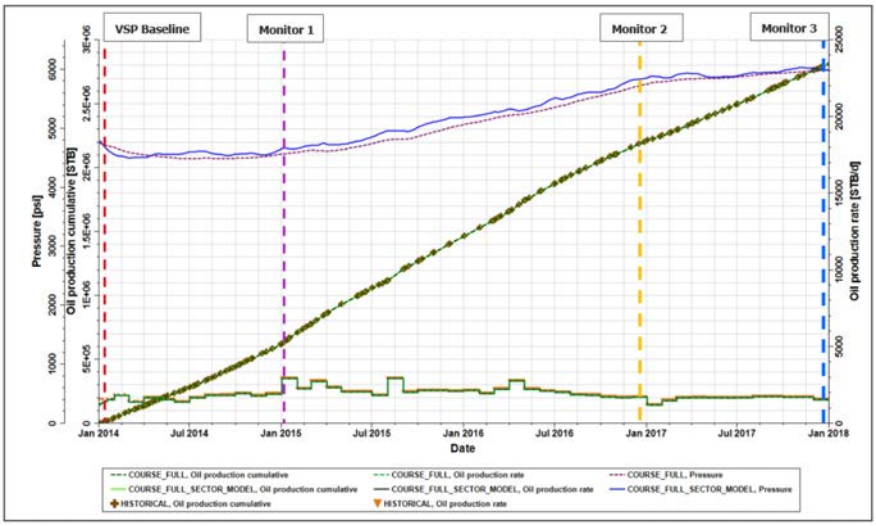

Figure 9—Calibrated compositional reservoir simulation covering the time-lapse VSP study.

The current study evaluates only the near-wellbore effects within the 1000 ft radius of the 13-10A well, and, as such, we utilize a sector model. Figure 9 compares the sector models' production history with the calibrated full field model and observed historical production, showing impeccable matches for oil production rate and cumulative oil production. (Note that the maximum injection pressure has been increased to match the recently acquired Bottom Hole Pressure). The simulated average pressure for the sector model shown as a solid blue line, which is slightly higher than that for the full field shown as a dashed purple line. Figure 9 also demarcates the baseline and monitor measurements where the fluid densities saturation and total compressibility are extracted to compute seismic velocities attributed to fluid substitution.

Seismic Velocity Attributed to Fluid substitution

The ongoing CO_2-WAG operations within the Morrow B inevitably induce changes in fluid saturation as produced oil is replaced by a mixture of water and CO_2. Figure 10 shows composite plots that illustrate the saturation evolution within the sector model at the baseline and at the monitor measurements. Red indicates gas saturation; the blue indicates water saturation, and the green shows oil.

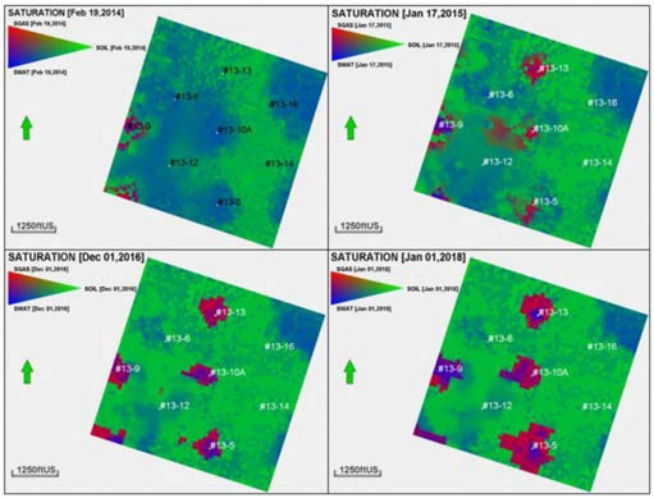

Figure 10—Snapshots of saturation within the compositional reservoir simulation sector model at Baseline, Monitor 1, Monitor2, and Monitor3. Saturation changes drive modifications in shear and compressional seismic velocities.

The 13-10A is the well of interest and is centrally located within the simulation sector boundary. The baseline measurement shows no CO_2 saturation near to the 13-10A as it was drilled in January 2014; however, every subsequent monitor measurement shows regions of higher gas saturations in the 13-10A near-wellbore region. This general pattern coincides with the evolution of observed shear and compressional seismic velocity (Figure 5).

Extracted fluid saturations and fluid densities are used along with the matrix porosity and matrix density to compute the bulk formation density according to equation 7. The shear modulus is unimpacted by the changes in fluid saturation, and as such, only bulk density changes drive alterations in the shear seismic velocity changes. Equation 5 indicates that any two shear seismic velocities can be related by the inverse of the square root of formation density change.

Figure 11 shows the delta-density for each monitor measurement computed relative to the baseline and compared to the shear seismic velocity impacts. Bright pink and blue regions on the areal distribution of delta density indicate reductions in bulk density. The areal extent of these specific regions correlates with increased time-lapse shear seismic velocity shown in bright red.

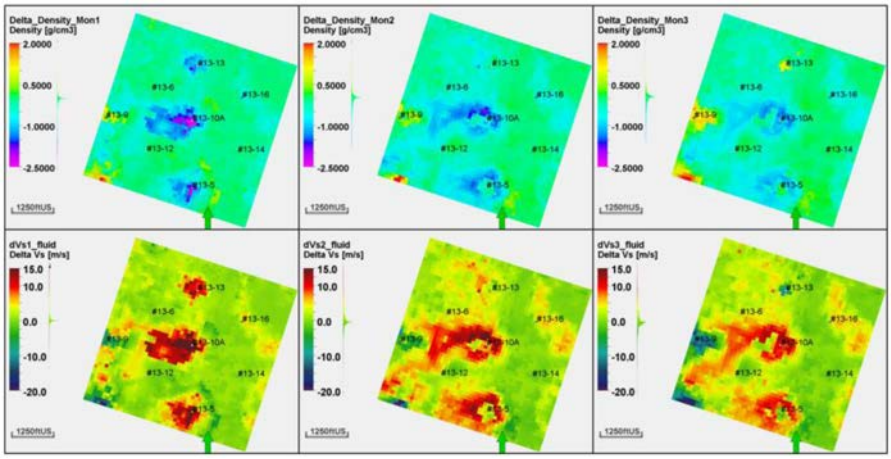

Figure 11—Time-lapse changes in formation bulk density (top) and time-lapse changes in shear-seismic velocity for every monitor time-step (relative to VSP Baseline).

These saturation distribution changes also impact the compressional seismic velocity through the fluid bulk modulus (K_f) and the bulk formation density (ρ). The relative impact of both variables determines the direction of the compressional seismic velocity change.

Figure 12 shows the relationship between delta-fluid-bulk modulus changes and the compressional seismic velocity each taken relative to the baseline measurements. The purple and blue in the delta-fluid-bulk modulus maps indicate regions of high gas saturation. High gas saturations cause reduced fluid bulk moduli and lower the saturated bulk modulus, which has the impact of lowering the compressional seismic velocity. The directional effect of changing bulk density is the same as that for the shear seismic velocity, but for this Morrow B CO_2-EOR operation, the bulk formation density has a less significant impact than the fluid compressibility effect.

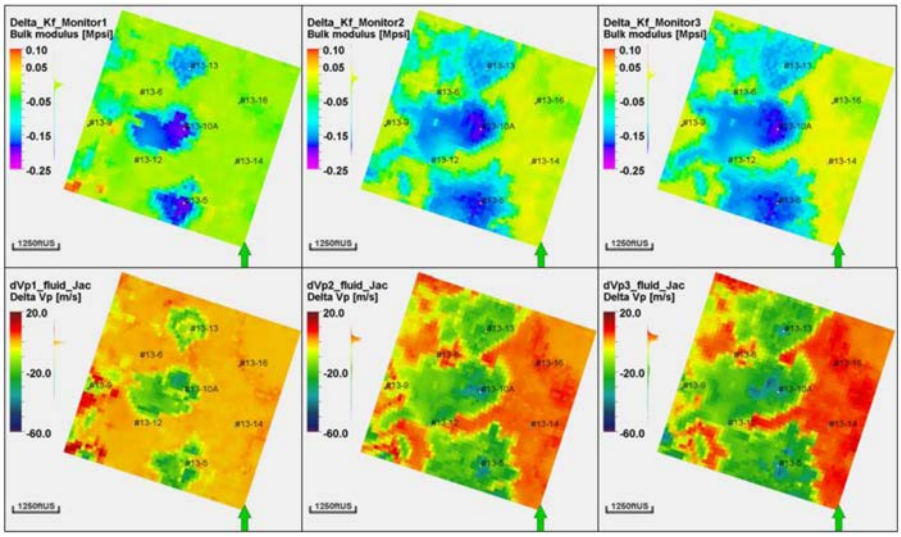

Figure 12—Shows the correlation between time-lapse changes in Bulk Modulus of the pore-filling fluid (top) and the Compressional Time-Lapse Seismic Velocity (relative to VSP Baseline) for Monitors 1, 2, and 3 (bottom row). The resulting compressional seismic velocity change is driven by the balance of formation bulk density change and that of the fluid bulk modulus.

Incidentally, the variations in compressional seismic velocity driven by fluid saturation changes delineate a channel crossing the north to the southeast portion of the modeled sector.

Coupled Hydrodynamic Geomechanical Simulation Model

The calibrated compositional reservoir simulation model is coupled one-way with the 3D mechanical earth coupled model (MEM). This model is the 4D rendering of stress changes induced by production and injection fluid influxes. Equation 13 shows that for one-way coupling, pressure increase results in a concomitant stress decrease. The production history match covering the time-lapse VSP study indicates a slight pore pressure decline from the baseline to monitor 1.

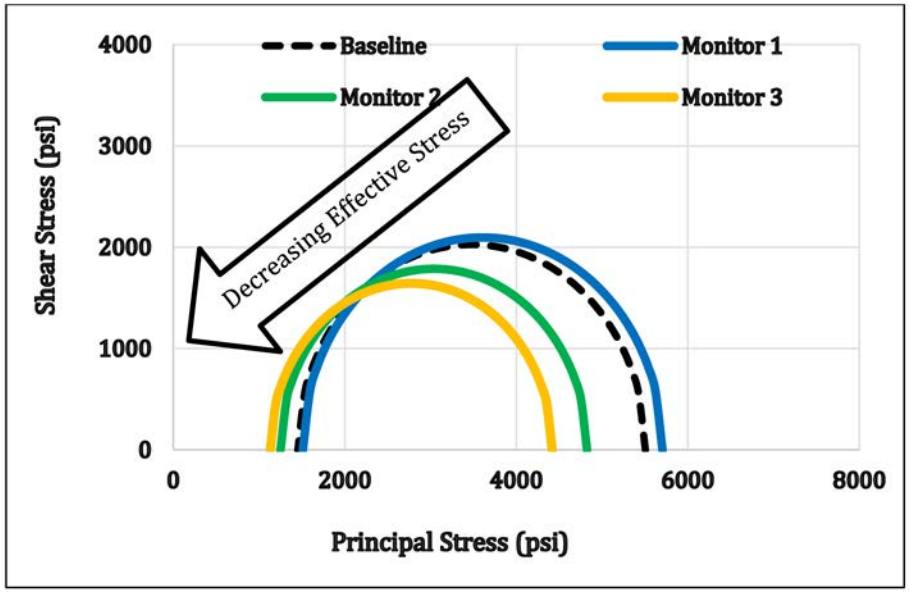

Figure 13—Mohr-Coulomb analysis for the during the VSP study. Mohr Circles coincide with the baseline and Monitor VSP.

The Mohr Circle for the geomechanical cell, which coincides with the 13-10A well is shown in Figure 13. The baseline stress state is shown as a dashed black semicircle. Monitor 1 is shown by the larger

blue semicircle indicating the expected increase in principal stress. Naturally, the increasing pore pressure observed at monitor 2 and monitor 3 result in lower stress states.

Seismic Velocity Change due to Stress State

Simulated effective stresses in the cartesian directions are extracted from the 4D geomechanical model to compute the mean effective stress at the baseline and for every monitor measurement. Ultrasonic testing on recovered Morrow B cores indicates a linear relationship between seismic velocities and effective stress once the mean effective stress is within the range of 1750 psi and 2750 psi. Differencing of baseline effective stress states from the effective stress at the monitor measurements yields the effective stress change. The change in effective stress is then directly correlated with shear and compressional seismic velocity changes.

Figure 14 shows the differences in mean effective stress, the associated changes in compressional seismic velocity, and shear wave velocity at every monitor measurement. The directions of the seismic velocity changes are consistent with those presented in the Mohr circle, meaning that a decrease in the mean effective stress relative to the baseline (monitor 2 and monitor 3) leads to a decrease in the both shear and compressional seismic velocity. The gradient for compressional seismic velocity is approximately 500 ft/sec (152.4 m/sec) per 1000 psi change in mean effective stress. The shear seismic velocity is approximately 40% of the compressional seismic velocity ratio.

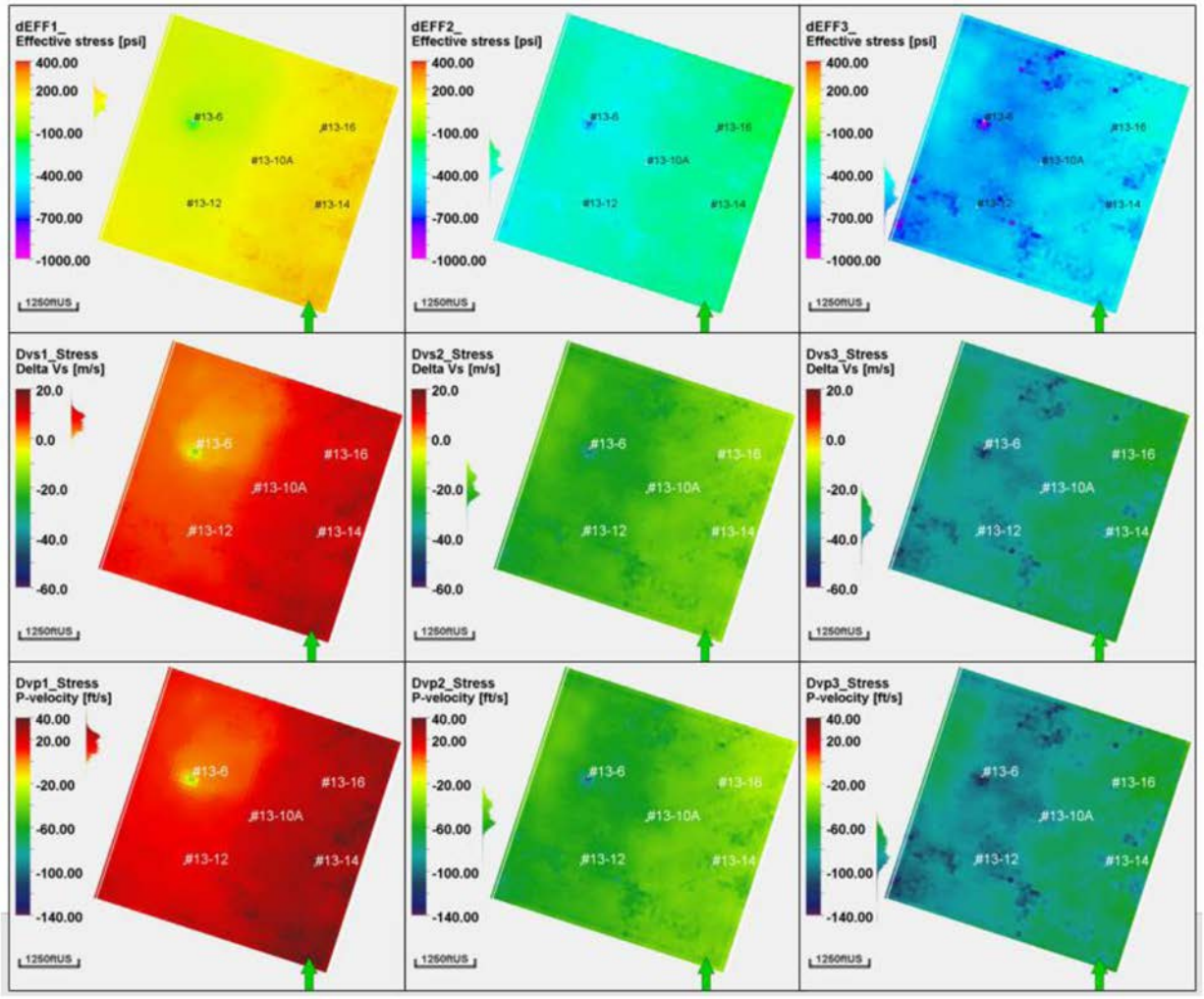

Figure 14—Changes in effective stress relative to the baseline, are generated by extracting results from the geomechanical simulation model. Results for Monitors 1, 2, and 3 are shown in the top row with the corresponding shear (middle row) and compressional seismic velocity (bottom row).

Interestingly, well #13-6 shows larger delta-effective stress changes with corresponding changes in shear and compressional seismic velocities. At the baseline simulation, pressure at the well #13-6 is exceptionally low. As all measurements are taken relative to the baseline, the large pressure and stress differential, show up in all computations that include the change in effective stress.

Penalty Function

Based on the principle of superposition, seismic velocity changes due to stress and that attributed to fluid substitution are linearly additive. The subsequent summation of seismic velocities, the scaling of modeled seismic velocity, and the differencing to form the mismatch are the next steps in the forward modeling process. Also of importance is constraining the observed dataset within its circle of validity. The observed dataset provided by time-lapse VSP measurements wanes in reliability with increasing distance away from the 13-10A well but is considered 100 % valid within the first 1000 ft.

Figure 15 shows the sum of the seismic velocity attributed to fluid substitution and that due to stress for the monitor 2 measurement. Comparison of the shear and compressional seismic velocity changes attributed to fluid substitution show that the regions of high gas saturation have positive shear seismic velocity changes, driven by the reduced bulk formation densities. A reverse trend is observed in compressional seismic velocity as the impacts of the increased gas saturation on the total fluid compressibility outweighs the effect of changes in the bulk formation density.

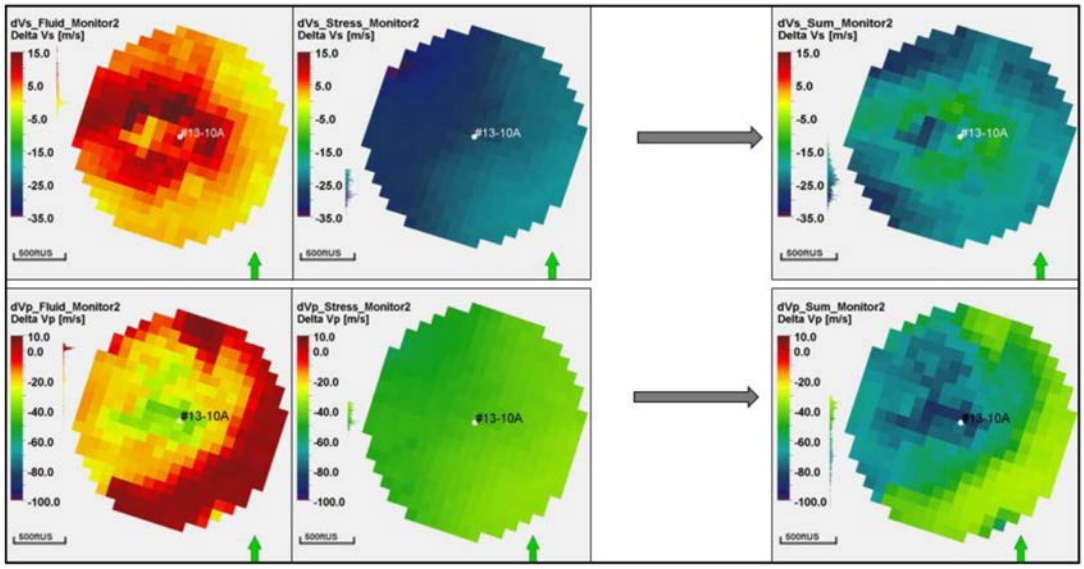

Figure 15—Summation of seismic velocity attributed to fluid substitution and that due to subsurface stress change for Monitor 2.

Patterns for the seismic velocity due to mean effective stress changes reflect the areal pressure distribution. Within the 1000 ft radius of the 13-10 A well, the seismic velocity decreases in a northwesterly direction, the reverse pattern of the pressure change. Seismic velocity changes due to effective stress change are computed based on the retrieved Morrow B core's stress sensitivity. While core tests provide valuable results, the age-old questions regarding the degree to which the retrieved core represents the reservoir interval remain present. Furthermore, while core measurements may be accurate under the testing conditions, they may not fully represent the reservoir's in situ response.

The relative contributions of seismic velocity change due to mean effective stress are larger than those attributed to fluid substitution for both the shear and compressional seismic velocity changes and for all monitor measurements. Figure 15 shows the seismic velocity changes at monitor 2. Modeled shear seismic velocity changes attributed to fluid substitution range from 15 m/s to -5 m/s and are driven by the reduced

bulk formation density as discussed in section 6.2. In contrast, shear seismic velocity change due to effective stress changes range from -21 m/s to -34 m/s, and are driven by increased pore pressure at the monitor 2 measurement.

Compressional seismic velocity changes due to effective stress changes are scaled relative to the shear seismic velocity changes and range from -35 m/s to -55 m/s. In comparison, fluid substitution contribution ranges from 5 m/s to -55 m/s and are impacted more by changes in fluid compressibility.

After summing the seismic velocity changes due to changes in effective stress and fluid substitution, the differences in scale between the reservoir and seismic resolution are addressed. The acoustic waves used in the time-lapse VSP acquisition have an estimated wavelength of 200-300 ft (60.96 m-91.44m) translating to a vertical resolution of 50 ft – 75 ft (15.24m-22.86m), which is much larger than the average Morrow B thickness-29 ft (8.84m). Backus averaging is applied to these modeled seismic velocities to reconcile scale differences before formulating the penalty function.

The next forward modeling step is creating the shear and compressional seismic velocity mismatch. The mismatches are created by differencing the "observed" seismic velocity inversion from the "modeled" (fluid substitution + stress) seismic velocity. Figure 16 shows that the observed shear seismic velocity changes at monitor 2 range from -7 m/s to -14m/s, much less negative than the modeled shear seismic velocity (-12.5 m/s to -32.5 m/s). Monitor 2 observed seismic velocity decreases towards the northeast as opposed to the pattern for the modeled shear seismic velocity: a circular pattern emanating from the central 13-10A well. The mismatch created for the monitor two (2) shear seismic velocity ranges from 2.5 m/s to -23 m/s.

Similarly, the modeled compressional seismic velocities have a much larger range than the observed. The observed compressional seismic velocities have a unique horseshoe pattern with negative seismic velocity (~ -25 m/s) at the 13-10A well, and extending to the northwest. This region is surrounded by much less negative changes in compressional seismic velocity. The mismatch created for the compressional seismic velocity has a very different areal pattern than the observed dataset.

Overall, Figure 16 shows variations in magnitudes for the shear and compressional seismic velocity mismatches, but much more significant are the differences in spatial seismic velocity patterns. These patterns result directly from the fluid saturation evolution and from the changes in the pressure distributions.

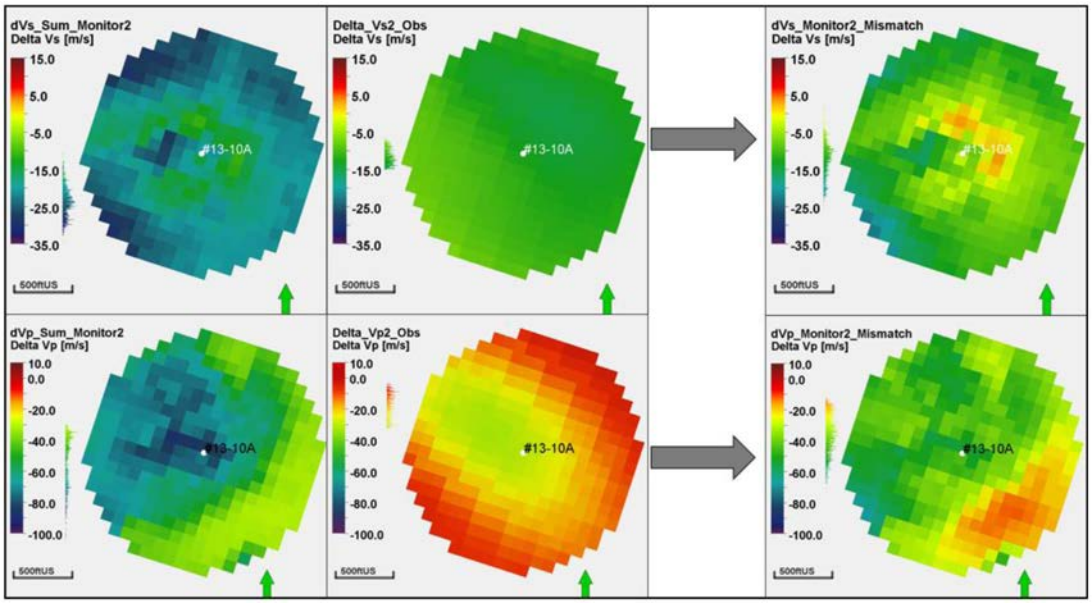

Figure 16—Mismatch created between 'modeled' and 'observed' seismic velocities for Monitor 2.

The penalty function is formed by the summation of all six (6) seismic velocity components representing the mismatch between the time-lapse shear and compressional seismic velocity changes for each of the

three monitor measurements. Future optimization work will be employed to minimize this mismatch thereby calibrating the coupled geomechanical simulation model.

Summary and Conclusions

The goal of the current work is the calibration of the coupled hydrodynamic geomechanical simulation model achieved in part by a VSP integration workflow. This project benefited from a novel elastic full-waveform inversion, site-specific rock physics model, and ultrasonic measurements on core, revealing measurable sensitivities to stress state changes. The thorough evaluation and utilization of this comprehensive dataset add validity to the predictions.

The observed time-lapse seismic velocity datasets show spatial and temporal expansions with increased CO_2 injection. The recognition that the time-lapse seismic velocity signatures carry the combined effect of saturation change and stress state change, and further that these seismic velocity changes are linearly additive, drives the VSP integration workflow.

The VSP integration workflow incorporated a calibrated compositional reservoir simulation, from which fluid properties are extracted to compute seismic velocity changes attributed to fluid saturation. Dry frame rock properties from the site-specific rock physics relationship complemented this process. Shear seismic velocity changes are related by the inverse of the square root of the formation bulk density change. The direction of compressional seismic velocity change is dependent on the relative influence of the fluid bulk modulus and formation bulk density. For the current CO_2-WAG, decreases in fluid bulk modulus result in decreasing compressional seismic velocities.

The hydrodynamic solution is coupled one-way with the 3D MEM to create a dynamic geomechanical simulation model that updated the stress state changes based on the hydrodynamic pressure distributions. Stress sensitivities derived from ultrasonic measurements on cores allow for the direct correlation between mean effective stress changes and shear and compressional seismic velocity change within a specified effective stress range. Ultimately, the shear seismic velocity changes due to stress are approximately 40% of the compressional seismic velocity change for this ongoing CO_2-WAG in the Morrow B.

Subsequent summing and scaling of the seismic velocities form the modeled portion of the penalty function, and differencing of observed from modeled seismic velocities form the mismatch in the seismic velocity domain.

The next critical steps are the 1:1 evaluation of input parameters to the penalty function and subsequent minimization of the seismic velocity mismatches. For the monitor 2 measurements, the shear seismic velocity mismatch is on the order of -10 m/s to -35 m/s while the compressional seismic velocity mismatch ranges from -30 m/s to -100 m/s. Stark differences also occur concerning the areal patterns of seismic velocity changes. The minimization of the seismic velocity mismatch holds the key to geomechanical model calibration as well as the answers regarding the suitability of time-lapse acoustic measurements for predicting changes in subsurface stress changes.

Future work

Future work will include implementing a machine learning assisted workflow to minimize the mismatch between the observed and modeled seismic velocities. Mismatch minimization is the next crucial step in achieving geomechanical calibration.

Acknowledgments

Funding for this project is provided by the U.S. Department of Energy's (DOE) National Energy Technology Laboratory (NETL) DOE Award No. DE-FE31684 and through the Southwest Regional Partnership on Carbon Sequestration (SWP) under and under DOE Award No. DE-FC26-05NT42591. Additional support has been provided by site operator Perdure Petroleum, L.L.C. and Schlumberger Carbon Services.

References

Ampomah, W., Balch, R., Grigg, R., Will, R., Dai, Z., & White, M. (2016). Farnsworth field CO 2-EOR project: performance case history. Paper presented at the SPE improved oil recovery conference.

Bachu, S. (2008). CO2 storage in geological media: Role, means, status and barriers to deployment. *Progress in energy and combustion science*, **34**(2), 254–273.

Batzle, M., & Wang, Z. (1992). Seismic properties of pore fluids. *Geophysics*, **57**(11), 1396-1408.

Ben van Beurden, C. o. S. (2020, Apr 16, 2020). Re: A NET-ZERO EMISSIONS ENERGY BUSINESS

Biot, M. A. (1955). Theory of elasticity and consolidation for a porous anisotropic solid. *Journal of applied physics*, **26**(2), 182–185.

Biot, M. A. (1956). Theory of propagation of elastic waves in a fluid-saturated porous solid. II. Higher frequency range. *The Journal of the acoustical Society of america*, **28**(2), 179-191.

Birch, F. (1961). The velocity of compressional waves in rocks to 10 kilobars: 2. *Journal of Geophysical Research*, **66**(7), 2199–2224.

Boot-Handford, M. E., Abanades, J. C., Anthony, E. J., Blunt, M. J., Brandani, S., Mac Dowell, N., … Hallett, J. P. (2014). Carbon capture and storage update. *Energy & Environmental Science*, **7**(1), 130–189.

De Coninck, H., Stephens, J. C., & Metz, B. (2009). Global learning on carbon capture and storage: A call for strong international cooperation on CCS demonstration. *Energy Policy*, **37**(6), 2161–2165.

Gallagher, S. R. (2014). Depositional and diagenetic controls on reservoir heterogeneity: upper morrow sandstone, Farnsworth unit, Ochiltree county, Texas. Citeseer,

Gao, K., & Huang, L. (2019). Acoustic-and elastic-waveform inversion with total generalized p-variation regularization. *Geophysical Journal International*, **218**(2), 933–957.

Gassmann, F. (1951). Elasticity of porous media. *Vierteljahrsschrder Naturforschenden Gesselschaft*, **96**, 1-23.

Geertsma, J. (1957). A remark on the analogy between thermoelasticity and the elasticity of saturated porous media. *Journal of the Mechanics and Physics of Solids*, **6**(1), 13–16.

Han, D.-h., Nur, A., & Morgan, D. (1986). Effects of porosity and clay content on wave velocities in sandstones. *Geophysics*, **51**(11), 2093–2107.

Hares, R. (2020). Feasibility of CCUS to CO2-EOR in Alberta.

Hawkes, C., McLellan, P., & Bachu, S. (2005). Geomechanical factors affecting geological storage of CO2 in depleted oil and gas reservoirs. *Journal of Canadian Petroleum Technology*, **44**(10).

Heddle, G., Herzog, H., & Klett, M. (2003). The economics of CO2 storage. Massachusetts Institute of Technology, Laboratory for Energy and the Environment.

Herwanger, J., & Horne, S. (2005). Predicting time-lapse stress effects in seismic data. *The Leading Edge*, **24**(12), 1234–1242.

Hillis, R. R. (2001). Coupled changes in pore pressure and stress in oil fields and sedimentary basins. *Petroleum Geoscience*, **7**(4), 419–425.

Hovorka, S., Mickler, P., Hosseini, S., Ganjdanesh, R., Nuñez-Lopez, V., Romanak, K., … Anderson, J. (2018). Monitoring Design for a Major US CCUS Project. Paper presented at the 14th Greenhouse Gas Control Technologies Conference Melbourne.

Huang, F., Juhlin, C., Kempka, T., Norden, B., & Zhang, F. (2015). Modeling 3D time-lapse seismic response induced by CO2 by integrating borehole and 3D seismic data–A case study at the Ketzin pilot site, Germany. *International Journal of Greenhouse Gas Control*, **36**, 66-77.

Jacobs, T. (2020). CO2 EOR Could Be Industry's Key to a Sustainable Future or Its Biggest Missed Opportunity. *Journal of Petroleum Technology*, **72**(11), 17–20.

Josu Jon Imaz, R. C. (2019). REPSOL WILL BE A NET ZERO EMISSIONS COMPANY BY 2050. In (pp. 6).

Kheshgi, H., de Coninck, H., & Kessels, J. (2012). Carbon dioxide capture and storage: Seven years after the IPCC special report. *Mitigation and Adaptation Strategies for Global Change*, **17**(6), 563–567.

Kokal, S., Sanni, M., & Alhashboul, A. (2016). Design and implementation of the first CO2-EOR demonstration project in Saudi Arabia. Paper presented at the SPE Annual Technical Conference and Exhibition.

Krief, M., Garat, J., Stellingwerff, J., & Ventre, J. (1990). A petrophysical interpretation using the velocities of P and S waves (full-waveform sonic). *The Log Analyst*, **31**(06).

McMillan, M., Will, R., Ampomah, W., Balch, R., & Czoski, P. (2019). Coupled Hydrodynamic-Geomechanical Modelling of CO2-WAG Field Development at Farnsworth Unit: A Case Study. Paper presented at the SPE Europec featured at 81st EAGE Conference and Exhibition.

Mechleri, E., Brown, S., Fennell, P. S., & Mac Dowell, N. (2017). CO2 capture and storage (CCS) cost reduction via infrastructure right-sizing. *Chemical Engineering Research and Design*, **119**, 130-139.

Morris, J. P., Hao, Y., Foxall, W., & McNab, W. (2011). A study of injection-induced mechanical deformation at the In Salah CO2 storage project. *International Journal of Greenhouse Gas Control*, **5**(2), 270–280.

Munson, T. W. (1988). Depositional, diagenetic, and production history of the Upper Morrowan Buckhaults Sandstone, Farnsworth Field, Ochiltree County Texas, Master's Thesis.

Núñez-López, V., & Moskal, E. (2019). Potential of CO2-EOR for near-term decarbonization. *Frontiers in Climate*, **1**, 5.

Olden, P., Corbett, P., Westerman, R., Somerville, J., Smart, B., & Koutsabeloulis, N. (2001). Modeling combined fluid and stress change effects in the seismic response of a producing hydrocarbon reservoir. *The Leading Edge*, **20**(10), 1154–1163.

Patrick Pouyanné, C. o. t. B. (2020). Total adopts a new Climate Ambition to Get to Net Zero by 2050. 2.

Ringrose, P., Mathieson, A., Wright, I., Selama, F., Hansen, O., Bissell, R., … Midgley, J. (2013). The In Salah CO2 storage project: lessons learned and knowledge transfer. *Energy Procedia*, **37**, 6226-6236.

Rose-Coss, D. (2017). A refined depositional sequence stratigraphic and structural model for the reservoir and caprock intervals at the Farnsworth Unit, Ochiltree County TX. New Mexico Institute of Mining and Technology,

Rose-Coss, D., Ampomah, W., Hutton, A. C., Gragg, E., Mozley, P., Balch, R. S., & Grigg, R. (2015). Geologic Characterization For CO 2-EOR Simulation: A Case Study of the Farnsworth Unit, Anadarko Basin, Texas. Paper presented at the AAPG Annual Convention and Exhibition.

Rubin, E., & De Coninck, H. (2005). IPCC special report on carbon dioxide capture and storage. UK: Cambridge University Press. TNO (2004): Cost Curves for CO2 Storage, Part, 2, 14.

Rutqvist, J., Vasco, D. W., & Myer, L. (2010). Coupled reservoir-geomechanical analysis of CO2 injection and ground deformations at In Salah, Algeria. *International Journal of Greenhouse Gas Control*, **4**(2), 225–230.

Skempton, A. (1961). Horizontal stresses in an overconsolidated Eocene clay. Paper presented at the Proc. of 5th Int. Conf. on SMFE.

Streit, J. E., & Hillis, R. R. (2004). Estimating fault stability and sustainable fluid pressures for underground storage of CO2 in porous rock. *Energy*, **29**(9-10), 1445-1456.

Suicmez, V. S. (2019). Feasibility study for carbon capture utilization and storage (CCUS) in the Danish North Sea. *Journal of Natural Gas Science and Engineering*, **68**, 102924.

Tosaya, C. A. (1983). Acoustical properties of clay-bearing rocks.

Trujillo, N. A. (2018). Influence of lithology and diagenesis on mechanical and sealing properties of the Thirteen Finger Limestone and Upper Morrow Shale, Farnsworth Unit, Ochiltree County, Texas: New Mexico Institute of Mining and Technology.

Vanorio, T., Prasad, M., & Nur, A. (2003). Elastic properties of dry clay mineral aggregates, suspensions and sandstones. *Geophysical Journal International*, **155**(1), 319–326.

Vidal, S., Huguet, F., & Mechler, P. (2002). Characterizing reservoir parameters by integrating seismic monitoring and geomechanics. *The Leading Edge*, **21**(3), 295–301.

Wilson, M., Monea, M., Whittaker, S., White, D., Law, D., & Chalaturnyk, R. (2004). IEA GHG Weyburn CO {sub 2} monitoring and storage project: summary report 2000-2004.

Wu, Z., Luhmann, A., Rinehart, A., Mozley, P., Dewers, T., Heath, J., & Majumdar, B. (2018). Controls of Cement Texture and Composition on Sandstone Mechanical Property Changes From Reaction With CO2-Rich Brine. Paper presented at the AAPG ACE 2018.